Modeling and Design of Periodic Polygonal Lattices Constructed from Microstructures with Varying Curvatures

Le Dong,[1] Dong Wang,[1,*] Jinqiang Wang,[1] Chengru Jiang,[1] Hui Wang,[2] Biao Zhang,[2,†] Mao See Wu,[3] and Guoying Gu[1,‡]

[1] *Robotics Institute and State Key Laboratory of Mechanical System and Vibration, School of Mechanical Engineering, Shanghai Jiao Tong University, Shanghai 200240, China*

[2] *Frontiers Science Center for Flexible Electronics (FSCFE), Xi'an Institute of Flexible Electronics (IFE) and Xi'an Institute of Biomedical Materials & Engineering (IBME), Northwestern Polytechnical University, 127 West Youyi Road, Xi'an 710072, China*

[3] *School of Mechanical and Aerospace Engineering, Nanyang Technological University, 50 Nanyang Avenue 639798, Singapore*

(Received 28 October 2021; revised 5 January 2022; accepted 25 March 2022; published 18 April 2022)

Lattice structures can exhibit unusual mechanical properties by appropriate design and arrangement of the microstructures, and have already found applications in areas such as tissue engineering, stretchable electronics, and soft robotics. However, the designed microstructures generally follow simple geometric patterns with constant curvatures and theoretical models are developed for each geometry particularly. It lacks a universal method to model and design the periodic lattice constructed from microstructures with varying curvatures. In this paper, we develop a universal approach to design polygonal lattices with a wide range of microstructures with varying curvatures using instant curvature and parametric functions. A finite deformation model is proposed for the microstructures and the corresponding lattices, which considers the wavy or curled microstructure, hierarchical geometry, and large deformation. Experiments and finite-element simulations are conducted to validate the theoretical model. All of Young's modulus, stretchability, and Poisson's ratio can be inversely designed using the developed theoretical model. Results show that the stretchability of the highly stretchable lattice can be further increased by more than 4 times using densely curled microstructure. The signs of Poisson's ratio can also change with the axial strain by rationally designing the microstructures. By combining curve fitting and curvature and parametric functions, the mechanical behaviors of lattices constructed by bioinspired microstructures can also be predicted. The lattice structures are then demonstrated to reinforce a hydrogel with modulus increased by around 2 orders and act as a biomimetic soft-strain sensor. This work could aid the design of a hierarchical lattice and have potential applications in tissue engineering, stretchable electronics, and soft robotics.

DOI: 10.1103/PhysRevApplied.17.044032

I. INTRODUCTION

Lattice structures, consisting of periodic arranged building blocks, exhibit exceptional properties and functionalities that differ from and surpass those of their constituent materials [1–9]. For example, honeycomb structures constructed by uniformly distributed double-layered hexagonal cells with high stiffness, strength, and energy absorption efficiency are developed [10,11]. Regular square grids reinforced by intersecting diagonal struts are proposed with potential applications in retarding crack propagation and increasing buckling strength [12].

*wang_dong@sjtu.edu.cn
†iambzhang@nwpu.edu.cn
‡guguoying@sjtu.edu.cn

Many biological materials exhibit high stretchability and strain-stiffening effect, preventing large deformations that may destroy tissue integrity, credited to wavy structures embedded in soft matrices [13,14]. Examples include blood vessels [15], mesentery tissue [16], human skin [17], lung parenchyma [18], cornea [19], and blood clots [20]. Inspired by the structures in biological materials, curved microstructures are used to replace the straight beams in artifical lattices to improve the mechanical properties. When the lattices are subjected to external loadings, the curved microstructures bend, rotate, uncurl, and align to the loading directions and resist excessive loadings by stretching. Therefore, the stretchabilities are significantly increased and they can simultaneously exhibit strain-stiffening behaviors with low initial modulus at small strain and high modulus at a large strain. Also, the lattices' mechanical properties, such as stretchability, elastic moduli, and Poisson's ratios (the negative ratio between lateral and longitudinal deformations of the whole lattice structure), can be tuned by varying the geometric parameters of the curved microstructures. Thus, they have found wide applications in areas where interactions with soft materials are necessary, such as in hydrogel reinforcement [21–26], stretchable electronics [27–30], and soft robotics [31–34].

For example, kagome [35], honeycomb [36], and hyperbolic lattices [37] have been designed to reinforce hydrogel in tissue engineering, in which the lattices' Young's moduli and Poisson's ratios are programmed to mimic those of the biological materials. To improve the stretchabilities of soft electronics, lattice structures with curved microstructures have been developed. Examples include rectangular and triangular horseshoe lattice structures [30,38], fractal-inspired constructs [27,39,40], Peano [41,42], Hilbert [27, 43], and Moore curves [27]. Due to the lightweight, shape-changing behaviors, and multifunctionalities, lattice structures with curved microstructures have also been used in soft robotics. For example, a magnetocapillary three-dimensional (3D) printed soft robot is fabricated to mimic creatures that live on the water's surface [5], which can exhibit different actuation modes, such as contraction, multiple shape changes, and functional reconfigurations, credited to its microstructures. Using the microstructure's buckling behavior, soft lattices that act as force switch, kinematic controller, and a pick and place end effector have been demonstrated [44]. A soft working robot that consists of two 3D-printed lattices with auxetic behavior is developed [45].

To further exploit the polygonal lattice structures, appropriate modeling and design approaches that take into account the microstructures' mechanical behaviors are needed. Several models are developed to model the mechanical behaviors of lattices constructed from various microstructures. For example, Ma *et al.* [46] proposed periodic lattices with horseshoe microstructures with constant curvatures and developed a finite deformation model to study their mechanical behaviors. Fan *et al.* [47] extended the horseshoe into serpentine microstructure by connecting the arcs with two straight beams. Zhang *et al.* [48] developed the fractal-inspired serpentine lattice and improved the stretchability by around 200 times via increasing the fractal order. Models for lattices with other types of microstructures have also been widely developed, such as straight beams [8,9], fractal horseshoe microstructures [39], zigzag microstructures [49], and sinusoidally curved microstructures [38]. In these previous research, the microstructures generally follow simple geometric patterns and models are developed for each geometry particularly. It lacks a universal method to model and design the periodic lattice constructed from microstructures with varying curvatures.

To circumvent this problem, we develop a general theoretical framework to design hierarchical lattice structures constructed from various microstructures in this paper, which takes into account the finite deformation of the complex microstructure and hierarchical structure. Two methods are used to design the microstructures with varying curvatures: (1) instant curvature (radius) function and (2) parametric function. Using the two methods, a wide range of wavy or curled microstructures and corresponding lattices can be built. The constructed rectangular and triangular lattices are shown in Figs. 1(a) and 1(b), respectively. Their mechanical behaviors under external loadings are investigated by combining finite deformation models, experiments, and finite-element (FE) simulations. The effects of geometric parameters are studied. The designed lattice structures are then demonstrated as a hydrogel reinforcement and a biomimetic soft-strain sensor.

This paper is presented as follows. In Sec. II, the theoretical model for the microstructures with varying curvatures is presented. The theoretical mechanical behaviors of lattices built from the microstructures are developed in Sec. III. Experiments and FE simulations are presented in Sec. IV. The effects of design parameters and demonstrations are shown in Sec. V. Conclusions are given in Sec. VI.

II. THEORETICAL MODEL OF MICROSTRUCTURES WITH VARYING CURVATURES

The mechanical behaviors of lattices strongly depend on their microstructures. Figure 1(a) and (b) show two methods to design the microstructures. In Fig. 1(c), the microstructure is formed using the relation between the instant radius $R(\alpha)$ and slope angle $\alpha (0 \le \alpha \le \alpha_{\text{end}})$. By directly using the curve function or parametric function, microstructures is constructed [Fig. 1(d)]. The full microstructures are shown in Figs. 1(e) and 1(f).

A. Microstructure designed by $R(\alpha)$

As schematically depicted in Fig. 2(a), when a hierarchical lattice structure is subjected to a uniaxial stretching, each microstructure undergoes antisymmetric deformation with respect to the central point [the black dot in Fig. 2(a)] due to the antisymmetricity. Therefore, based on previous studies [46,50], we consider that the microstructure is simply supported [Fig. 2(a)]. A horizontal force F_x and a vertical force F_y are applied at each end of the microstructure, and a pair of moments M_0 are antisymmetrically located at the ends. Only half of the microstructure is analyzed due to the antisymmetricity, as shown in Figs. 2(b) and 2(c). It should be noted that besides the local deformation of the microstructure, it also undergoes rigid body motions, which is taken into account in the theoretical model of lattice structures in Sec. III.

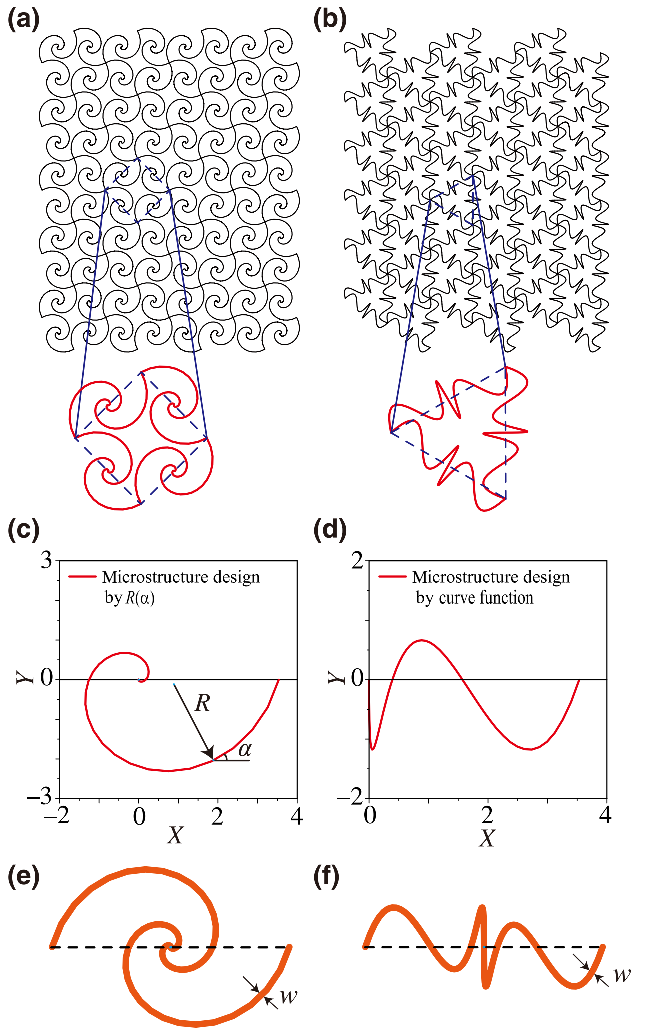

FIG. 1. Geometries of the lattice structures. Schematics of a (a) rectangular, (b) triangular and their periodic units. Their microstructures are constructed by the instant curvature $R(\alpha)$ (c) and by the curve function (d), respectively. The geometrical parameters for the microstructures are shown in (e),(f).

Figure 2(d) describes an infinitesimal curved segment of the microstructure in the undeformed and deformed configurations, represented in the X-Y and x-y coordinates, respectively. In the undeformed configuration, the slope angle $\alpha(0 \leq \alpha \leq \alpha_{\text{end}})$ is defined as the angle between the centroid axis and horizontal line. In the deformed configuration, α becomes $\theta(\theta_0 \leq \theta \leq \theta_{\text{end}})$. Therefore, the rotational angle φ resulting from the deformation is $\theta - \alpha$. Under stretching, the length of the infinitesimal segment at the centroid axis varies from dS to ds, and the engineering strain at the centroid axis is $\varepsilon = (ds - dS)/dS$, where $dS = R(\alpha)d\alpha$ and $ds = r(\theta)d\theta$. $R(\alpha)$ is the radius of the arc in the microstructure at the undeformed configuration, and $r(\theta)$ denotes the radius of the deformed arc.

The axial force N, the shear force Q, and the bending moment M at any cross section [Fig. 2(e)] can satisfy the following equilibrium equations [51]:

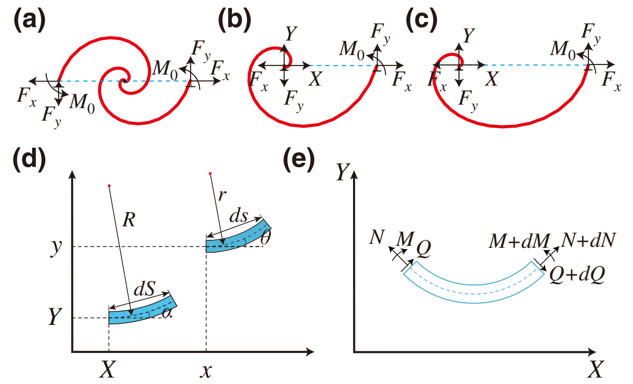

FIG. 2. Force analysis of a single microstructure. (a) Schematics of a microstructure under an axial force F_x, a shear force F_y, and a moment M_0 at two ends. (b) Half of the microstructure under F_x, F_y, and M_0. (c) Schematics of the deformed shape of half of the microstructure. (d) Deformation of a length element. (e) Force and moment sign conventions.

$$\frac{dN}{ds} + \frac{Q}{r} = 0, \quad -\frac{N}{r} + \frac{dQ}{ds} = 0, \quad \frac{dM}{ds} = Q, \quad (1)$$

where $N = EA\varepsilon, M = EI(1+\varepsilon)d\varphi/ds = EI(d\varphi/dS)$, E is Young's modulus, $A = w \times d$ the cross-section area of the microstructure, and I ($I = w^3 d/12$) is the second area moment. d represents the thickness in the Z direction, and w represents the width of a microstructure. The axial and shear forces can then be calculated using the loading conditions as

$$N = F_x \cos\theta + F_y \sin\theta, \quad Q = F_x \sin\theta - F_y \cos\theta. \quad (2)$$

Substituting Eq. (2) into Eq. (1), $d^2\varphi/dS^2$ can be rewritten as

$$\frac{d^2\varphi}{dS^2} = f(\theta), \quad (3)$$

where $f(\theta) = \left(EA + F_x \cos\theta + F_y \sin\theta\right) \times (F_x \sin\theta - F_y \cos\theta\big) / (EI \times EA)$.

In the undeformed arc, $dS = R(\alpha)d\alpha$. Equation (3) can be written as

$$\frac{d^2\varphi}{dS^2} = \frac{1}{R}\left(\frac{d(R^{-1})}{d\alpha}\frac{d\varphi}{d\alpha} + R^{-1}\frac{d^2\varphi}{d\alpha^2}\right). \quad (4)$$

By using Eqs. (3) and (4),

$$\frac{d^2\varphi}{d\alpha^2} = -R\frac{d(R^{-1})}{d\alpha}\frac{d\varphi}{d\alpha} + R^2 f(\theta). \quad (5)$$

From $\theta = \alpha + \varphi$, we can get

$$\frac{d\varphi}{d\alpha} = \frac{d\theta}{d\alpha} - 1 \text{ and } \frac{d^2\varphi}{d\alpha^2} = \frac{d^2\theta}{d\alpha^2}. \quad (6)$$

Thus, the governing equation, Eq. (5), can be written as a differential equation of θ as

$$\frac{d^2\theta}{d\alpha^2} = -R\frac{d(R^{-1})}{d\alpha}\left(\frac{d\theta}{d\alpha} - 1\right) + R^2 f(\theta), \qquad (7)$$

with the following two boundary conditions:

$$\text{(BC1)}\ \frac{d\theta}{d\alpha}(\alpha = \alpha_0) = 1, \qquad (8)$$

$$\text{(BC2)}\ l_y = \int \sin\theta ds = 0. \qquad (9)$$

It should be noted that (BC1) implies null moment of the central point, as only half of the microstructure is considered. Recalling that $ds = (1+\varepsilon)dS, dS = R(\alpha)d\alpha$, (BC2) can be written as

$$l_y = \int_{\alpha_0}^{\alpha_{\text{end}}} (1+\varepsilon)R(\alpha)\sin\theta d\alpha = 0. \qquad (10)$$

Equations (7), (8), and (10) are second-order ordinary differential equations with two boundary conditions, in which (BC2) is an integral boundary condition. The ordinary differential equation can be solved numerically. After the relationship between θ and α is obtained, the deformed shape can be constructed using the following integrations:

$$x = \int_{\theta_0}^{\theta} r(\theta)\cos\theta d\theta, \qquad (11)$$

$$y = \int_{\theta_0}^{\theta} r(\theta)\sin\theta d\theta, \qquad (12)$$

where $\theta_0 \le \theta \le \theta_{\text{end}}$.

B. Microstructures designed by parametric functions

We next extend the theory to microstructures constructed by parametric functions. For this type of microstructure, the relationship between the instant curvature and radius and the slope angle is not given explicitly. Instead, both of them are expressed as a function of the parametrization parameter. A two-dimensional (2D) curve in the undeformed state can be represented by the following parametrization:

$$X = \psi(t), \qquad (13)$$

$$Y = \zeta(t), \qquad (14)$$

where t ($t_0 \le t \le t_{\text{end}}$) is a parameter. The radius of the curve can then be written as

$$R(t) = \frac{[\psi'^2(t) + \zeta'^2(t)]^{\frac{3}{2}}}{[\psi'(t)\zeta''(t) - \psi''(t)\zeta'(t)]}, \qquad (15)$$

where the prime denotes the differentiation with respect to t. The slope angle $\alpha(t)$ can be obtained by

$$\tan[\alpha(t)] = \frac{\zeta'(t)}{\psi'(t)}. \qquad (16)$$

Substituting Eqs. (15) and (16) into Eqs. (5) and (6), we can obtain

$$\frac{d^2\varphi}{d\alpha^2} = \frac{R'}{R\alpha'}\frac{d\varphi}{d\alpha} + R^2 f(\theta), \qquad (17)$$

$$\frac{d\varphi}{d\alpha} = \frac{d\theta}{d\alpha} - 1 = \frac{\theta'}{\alpha'} - 1 \text{ and } \frac{d^2\varphi}{d\alpha^2} = \frac{d^2\theta}{d\alpha^2} = \frac{\theta''\alpha' - \theta'\alpha''}{\alpha'^3}. \qquad (18)$$

Thus, the governing equation, Eq. (17), can be written as

$$\theta'' = (\theta' - \alpha')\frac{R'}{R} + R^2\alpha'^2 f(\theta) + \frac{\theta'\alpha''}{\alpha'}. \qquad (19)$$

The two boundary conditions Eqs. (8) and (10) become

$$\text{(BC1)}\ \theta'(t_0) = \alpha'(t_0), \qquad (20)$$

$$\text{(BC2)}\ l_y = \int_{t_0}^{t_{\text{end}}} (1+\varepsilon)R\sin\theta\alpha' dt = 0. \qquad (21)$$

By substituting the expression of α in Eq. (16) into Eq. (19), the second-order ordinary differential equation of θ with respect to t can then be solved using MATLAB with the above two BCs.

III. THEORETICAL MODEL FOR THE HIERARCHICAL LATTICE STRUCTURES

In this section, the theoretical model for the lattice structures built from the microstructures with varying curvatures is presented. Three types of polygonal lattice structures are shown as examples: the rectangular lattice, the triangular lattice (details given in Fig. S1 within the Supplemental Material [52]), and the symmetric rectangular lattice. The force analysis is shown in Fig. 3. The theoretical model of other polygonal lattices can be derived similarly.

A. Rectangular lattice

We investigate the deformation of a rectangular hierarchical lattice structure under uniaxial vertical stress σ. Each representative unit cell consists of four microstructures, indexed from 1 to 4, as shown in Figs. 3(a) and 3(c). β_1 and β_2 characterize the rigid-body motion of each microstructure. Due to the representative unit's antisymmetricity around its central point, the inner force, moment, and deformation of microstructures 1 and 3 are the same, and those of microstructures 2 and 4 are the same. The

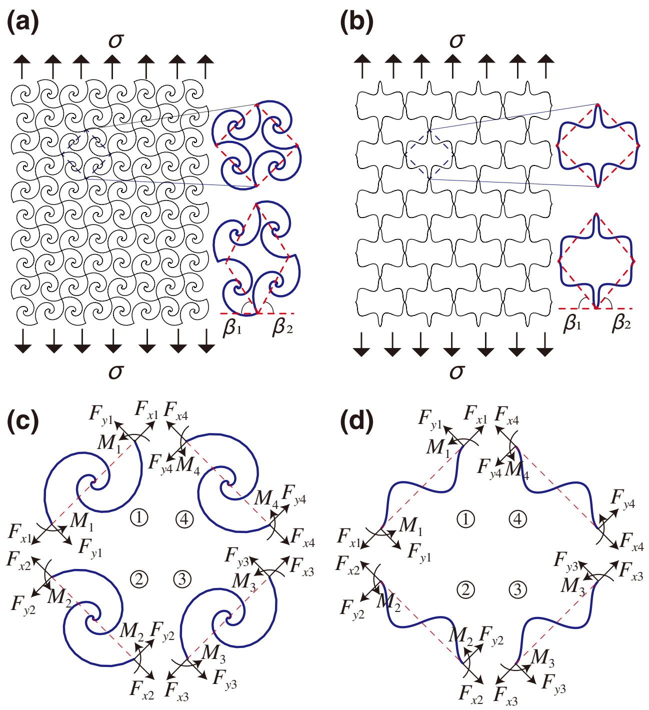

FIG. 3. Schematics of a (a) rectangular and (b) symmetric rectangular lattice under uniaxial vertical stress σ. The undeformed and deformed shapes of a representative unit are shown. Inner forces and moments for each microstructure in the representative units are shown in (c),(d), respectively.

static equilibrium of the representative unit requires that the inner force at the joint between microstructure 1 and 2 is zero in both X and Y directions, which yields

$$F_{x1}\cos\beta_2 - F_{y1}\sin\beta_2 + F_{x2}\cos\beta_1 + F_{y2}\sin\beta_1 = 0, \tag{22}$$

$$F_{x2}\sin\beta_1 - F_{x1}\sin\beta_2 - F_{y1}\cos\beta_2 - F_{y2}\cos\beta_1 = 0. \tag{23}$$

The external loading on the representative unit is σ. Thus it can be obtained in the Y direction:

$$F_{x1}\sin\beta_2 + F_{y1}\cos\beta_2 + F_{x2}\sin\beta_1 - F_{y2}\cos\beta_1 = 4\sqrt{2}\sigma Rd, \tag{24}$$

and in the X direction:

$$-F_{x1}\cos\beta_2 + F_{y1}\sin\beta_2 + F_{x2}\cos\beta_1 + F_{y2}\sin\beta_1 = 0. \tag{25}$$

The moment equilibrium of an arbitrary joint, which is connected by four microstructures, and the antisymmetry requires that

$$\sum_{i=1}^{4} M_i = -\sum_{i=1}^{4}(F_{yi}L_i)/2 = 0. \tag{26}$$

The angle between the tangent directions of two connected microstructures remains unchanged during deformation. Thus we have

$$\beta_1 + \beta_2 + \theta_1 - \theta_2 = \pi/2. \tag{27}$$

For each microstructure 1 or 2, the relationship between its deformation and the applied loadings are given in Eq. (7) with two BCs Eqs. (8) and (10) or Eq. (19) with two BCs Eqs. (20) and (21). The spanning length in the X direction is given by

$$L_i = \int_0^{\alpha_{\mathrm{end}}}(1+\varepsilon)R(\alpha)\cos\theta_i d\alpha \tag{28}$$

for microstructures constructed by $R(\alpha)$ or

$$L_i = \int_{t_0}^{t_{\mathrm{end}}}(1+\varepsilon)R\cos\theta_i\alpha' dt \tag{29}$$

for microstructure constructed by parametric functions, where $i = 1$ or 2. By using $F_{x3} = F_{x1}$, $F_{x4} = F_{x2}$, $F_{y3} = F_{y1}$, and $F_{y4} = F_{y2}$, and solving the above ten equations, the ten unknowns F_{x1}, F_{x2}, F_{y1}, F_{y2}, θ_1, θ_2, L_1, L_2, β_1, and β_2 can be solved.

B. Symmetric rectangular lattice

Symmetrical rectangular hierarchical lattice structure under uniaxial vertical stress σ is studied. Each representative unit cell consists of four microstructures, indexed from 1 to 4, as shown in Figs. 3(b) and 3(d). Due to the representative unit's symmetry around its central point, the inner force, moment, and deformation of microstructures are the same or axisymmetric. For microstructures 1 and 2, we have

$$F_{x1} = F_{x2}, \tag{30}$$

$$F_{y1} = -F_{y2}, \tag{31}$$

$$\beta_1 = \beta_2, \tag{32}$$

$$L_1 = L_2, \tag{33}$$

$$\theta_1 = \theta_2. \tag{34}$$

The static equilibrium of the representative unit requires that the inner force at the joint between microstructure 1 and 2 is zero in both X and Y directions, which yields

$$F_{x1}\cos\beta_2 - F_{y1}\sin\beta_2 + F_{x2}\cos\beta_1 + F_{y2}\sin\beta_1 = 0, \tag{35}$$

$$F_{x2}\sin\beta_1 - F_{x1}\sin\beta_2 - F_{y1}\cos\beta_2 - F_{y2}\cos\beta_1 = 0. \tag{36}$$

The external loading on the representative unit is σ. Thus it can be obtained in the Y direction:

$$\begin{aligned} &F_{x1}\sin\beta_2 + F_{y1}\cos\beta_2 + F_{x2}\sin\beta_1 - F_{y2}\cos\beta_1 \\ &\quad = 4\sqrt{2}\sigma Rd, \end{aligned} \tag{37}$$

and in the X direction:

$$-F_{x1}\cos\beta_2 + F_{y1}\sin\beta_2 + F_{x2}\cos\beta_1 + F_{y2}\sin\beta_1 = 0. \tag{38}$$

The moment equilibrium of an arbitrary joint, which is connected by four microstructures, requires that

$$\sum_{i=1}^{4} M_i = -\sum_{i=1}^{4} (F_{yi}L_i)/2 = 0. \tag{39}$$

The angle between the tangent directions of two connected microstructures remains unchanged during deformation. Thus we have

$$\theta_2 - \beta_1 = \theta_1 - \beta_2 = \theta_0 - \pi/4, \tag{40}$$

where θ_0 can be obtained when symmetrical rectangular hierarchical lattice structure under $\sigma = 0$. Following the similar procedures, the ten unknowns F_{x1}, F_{x2}, F_{y1}, F_{y2}, θ_1, θ_2, L_1, L_2, β_1, and β_2 can be solved.

IV. VALIDATION OF THE THEORETICAL MODEL

In this section, the theoretical model is compared with the FE simulations and experimental results (Videos S1–S3 within the Supplemental Material [52]). Three structures are designed: a rectangular lattice, a triangular lattice, and a symmetric rectangular lattice. The microstructure of the rectangular lattice is designed using $R(\alpha)$, where $R(\alpha) = \alpha^3 + \alpha^2 + \alpha - 1, 0 \le \alpha \le 7.5$. The microstructure of the triangular lattice is designed using a parametric function with $X(t) = t^2\cos(t)$, $Y(t) = t^2\sin(t)$, where $0 \le t \le \pi$. The symmetric lattice's microstructure is designed by a parametric function $Y(X) = X(X-1)^2, 0 \le X \le 1$, as shown in Fig. 4(i).

The curved structures pose significant challenges for manufacturing. High-resolution 3D printing is an appropriate way to fabricate the complex lattice. In this work, we use a commercial Polyjet 3D printer (Stratasys, Connex 500) with a resolution of around 100 μm. To ensure the designed lattice can be fabricated, the width of the microstructure w is set to be larger or equal to 0.2 mm, and enough void (0.1 mm) between microstructures is kept to avoid self-intersection during printing. However, the manufacturing of microstructures with more complex and finer structures is still hindered, which may be overcome by the rapid development of additive manufacturing.

VeroWhite is chosen as the material with Young's modulus $E = 1.2$ GPa. For simplicity, VeroWhite will be referred to as Vero. All of the microstructures are scaled to $L = 5\sqrt{2}$ mm. The width $w = 0.2$ mm and the thickness $d = 3$ mm. Five periodic units in the horizontal and eight units in the vertical direction are used in the rectangular and symmetric rectangular lattice, respectively. Six units and eight units are used for the triangular lattice in the horizontal and vertical directions. The loading speed of rectangular and symmetric lattice is 15 mm/min and the loading speed of triangular lattice is 5 mm/min in experiments. The FE details are given in Sec. S7 within the Supplemental Material [52].

The experimental, theoretical, and FE simulated uniaxial tensile test results are shown in Fig. 4. It can be seen that (1) all of the lattice structures exhibit a J-shaped tensile curve, i.e., a low effective modulus at the "toe" region and a large modulus at the "linear region"; (2) under the same tensile stress, the rectangular lattice is easiest to be stretched, while the triangular lattice is hardest to be stretched. For example, when $\sigma = 30$ kPa, the axial strains of the rectangular, triangular, and symmetric lattices are around 125%, 25%, and 30%, respectively; (3) an obvious transition point can be observed. The deformed theoretical (black dashed), experimental (blue solid) and FE simulated (red dashed) shapes of the rectangular, triangular, and symmetric lattices with various strains are presented.

All theoretical, experimental, and FE deformed shapes agree well when the strain is less than 125% for rectangular lattice, 30% for triangular lattice, and 25% for symmetric lattice. There are some discrepancies when the strain is large. The experimental curves are lower than theoretical results in Fig. 4(e), which is mainly due to the plastic deformation. The uniaxial tensile stress-strain curve of Vero is shown in Fig. S6 within the Supplemental Material [52]. It shows a plastic behavior when the strain is larger than 5%. The boundary effect is relatively less as Poisson's ratio of the lattice is nearly zero. From Figs. 4(g) and 4(h), we can observe that the vertical microstructures of the triangular lattice are almost pulled straight. Additional plastic deformation exists, which leads to a larger displacement compared to the theoretical results, when the same stress is applied.

The experimental curves are higher than theoretical results in Fig. 4(i). For the symmetric lattice [Figs. 4(k) and 4(l)], the discrepancy results mainly from the

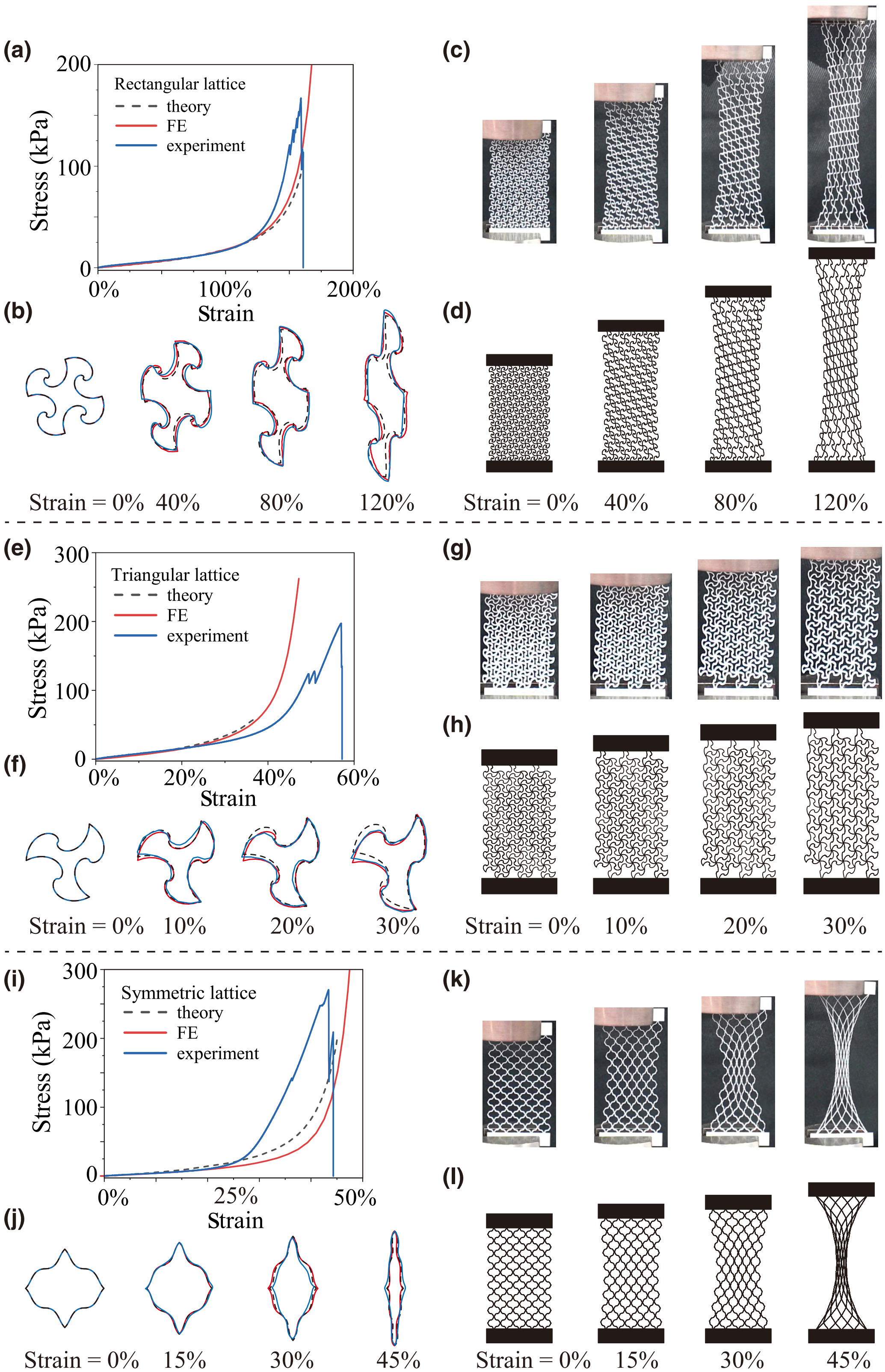

FIG. 4. Comparison of the experimental, theoretical, and FE simulated results. (a) shows the experimental, theoretical, and FE simulated uniaxial tensile curves of a rectangular lattice. The theoretically predicted, experimental, and FE simulated deformed shapes of a representative unit are shown in (b). (c),(d) show the experimental and FE simulated deformed shapes at various strains. The experimental, theoretical, and FE simulated uniaxial tensile curves of a triangular lattice are shown in (e). The deformed shapes of a representative unit are shown in (f). The experimental and FE simulated snapshots are shown in (g),(h). The comparisons between the theoretical, experimental, and FE simulated tensile curves of a symmetric rectangular lattice are shown in (i). The deformed representative units of the symmetric rectangular lattice are shown in (j). (k),(l) show the experimental and FE simulated snapshots.

boundary effect. The boundary effect dominates due to the large Poisson’s ratio. The lattice at the boundaries is almost straight, which contributes significantly larger stress. Thus the experimental curves are above the theoretical results.

To decrease the discrepancies, we need to reduce the boundary effects and plastic deformation. To decrease plastic deformation, excess stretch needs to be avoided. For a lattice with a large magnitude of Poisson’s ratios, the boundary effect is generally large. Therefore, we can use the lattice with loose boundary constraints or with nearly zero Poisson's ratio to replace the boundary part to mitigate the boundary effects. The discrepancy between the FE simulations and the experimental results may be due to the use of the wire element in the FE simulations. We show in Fig. S7 within the Supplemental Material that the discrepancy between the FE and experimental results decreases by using the shell element. It should also be mentioned that replacing the point corners with rounded corners reduces stress concentration, and the structures become more reliable.

Self-contact may also be one factor of the discrepancy. To avoid self-contact, we give enough space between microstructures during the initial design, as shown in Fig. S2 within the Supplemental Material [52]. However, self-contact is inevitable for lattices with large positive Poisson's ratios, especially when the axial strain is large and the microstructure is super-curled, as shown by examples in Fig. 4(k). As the self-contact generally happens at very large strains before failure, it does not violate the applicability of the theoretical model.

There are currently no standard tensile testing structures for lattices. Therefore, we still use the regular lattice structures in the experiments, following previous works [46,49]. To reduce the boundary effect in the experiments, we fabricate lattices with relatively large aspect ratios (length and width) and choose the central periodic unit with the lowest boundary effect in comparison with theoretical models. However, the boundary effect cannot be eliminated and causes discrepancies. Designing standard tensile test structures for lattices is an interesting topic. Future work can be done in this area to reduce the boundary effects in experimental tests.

V. DESIGN OF HIERARCHICAL LATTICES

In this section, the validated model is used to design the microstructure and the corresponding hierarchical lattice structures. Their stress-strain and Poisson's ratio-strain curves are particularly investigated. Besides the lattice designed by curvature and parametric functions, lattices constructed by bioinspired microstructures are also studied. The applications of lattices as hydrogel reinforcement and biomimetic soft lattice sensor are demonstrated. All of the microstructures are scaled to $L = 5\sqrt{2}$ mm. The width $w = 0.133$ mm and the thickness $d = 1$ mm, unless otherwise specified. Young's modulus of the material is set as $E = 1.2$ GPa.

A. Design by varying the range of α

Three different microstructures are designed using the same function $R(\alpha) = \alpha^3 + \alpha^2 + \alpha - 1, 0 \leq \alpha \leq \alpha_{\text{end}}$, but with varying $\alpha_{\text{end}} = \alpha_1(3.9), \alpha_2(7.5)$, and $\alpha_3(10.7)$. The microstructures' initial shapes are shown in Fig. 5(a), while the undeformed constructed rectangular lattices are shown in Fig. 5(b). The structure with larger α_{end} shows a larger density.

The theoretical predicted stress-strain and Poisson's ratio-strain curves of the three designed lattices under uniaxial tensile loading are shown in Figs. 5(d) and 5(e), respectively. FE simulated results are shown by the markers. The undeformed and deformed shapes of a representative unit of the three lattices under $\sigma = 10$ kPa are shown in Fig. 5(c). It can be seen that the structures with larger α are easier to stretch, even though they exhibit the largest density. For example, at $\sigma = 10$ kPa, the lattice with $\alpha_{\text{end}} = 3.9$ shows only a strain less than 40% [Fig. 5(c)-I], while the axial strain of the lattice with $\alpha_{\text{end}} = 10.7$ [Fig. 5(c)-III] is larger than 175%. By increasing α_{end} from 3.9 to 10.7, the stretchability increases by more than 4 times when the same stress is applied. Poisson's ratios are all positive and gradually decrease with α_{end}. Poisson's ratio of the lattice with $\alpha_{\text{end}} = a_1(3.9)$, exceeds the upper limit 0.5 of traditional material [53], which is one advantage of the lattice structures.

The value of α_{end} controls the curling degree of the microstructure. By increasing α_{end}, the curling area of the microstructure increases, which shows a higher density. When the lattice is subjected to an axial loading, the curling microstructure will be pulled straight. Thus, lattice designed with a larger α_{end} will lead to a larger stretchability. Another two examples of design by the curvature functions are shown in Figs. S3 and S4 within the Supplemental Material [52].

B. Design by parametric curves

The microstructures are designed by directly using parametric function $Y(X) = C_n X(X - n)$, with $n = 0.5, 1, 1.5, 2, 2.5$, and 3 in Fig. 6. The corresponding microstructures are shown in Fig. 6(a). The span length of the microstructure is scaled to $L = 5\sqrt{2}$ mm, by using the coefficient C_n. Both rectangular and triangular lattices are designed, as shown in Figs. 6(b) and 6(c).

The stress-strain and Poisson's ratio-strain curves of the rectangular lattice under uniaxial loading are shown in Figs. 6(d) and 6(e), respectively. It can be seen that the strain of the lattice increases with n, as the microstructure becomes easier to stretch due to the increase of the curve amplitude. Poisson's ratios of the rectangular lattices are positive and decrease with n. The triangular lattice's mechanical behaviors are shown in Figs. 6(h) and 6(i). Similar to the rectangular lattice, the stretchability of the triangular lattice increases with n. The transverse strain of the designed triangular lattices are always positive, indicating a negative Poisson's ratio. For lattice with $n \geq 1.5$, it can be observed that the magnitude of Poisson's ratio decreases with the strain until it reaches a minimum. As the

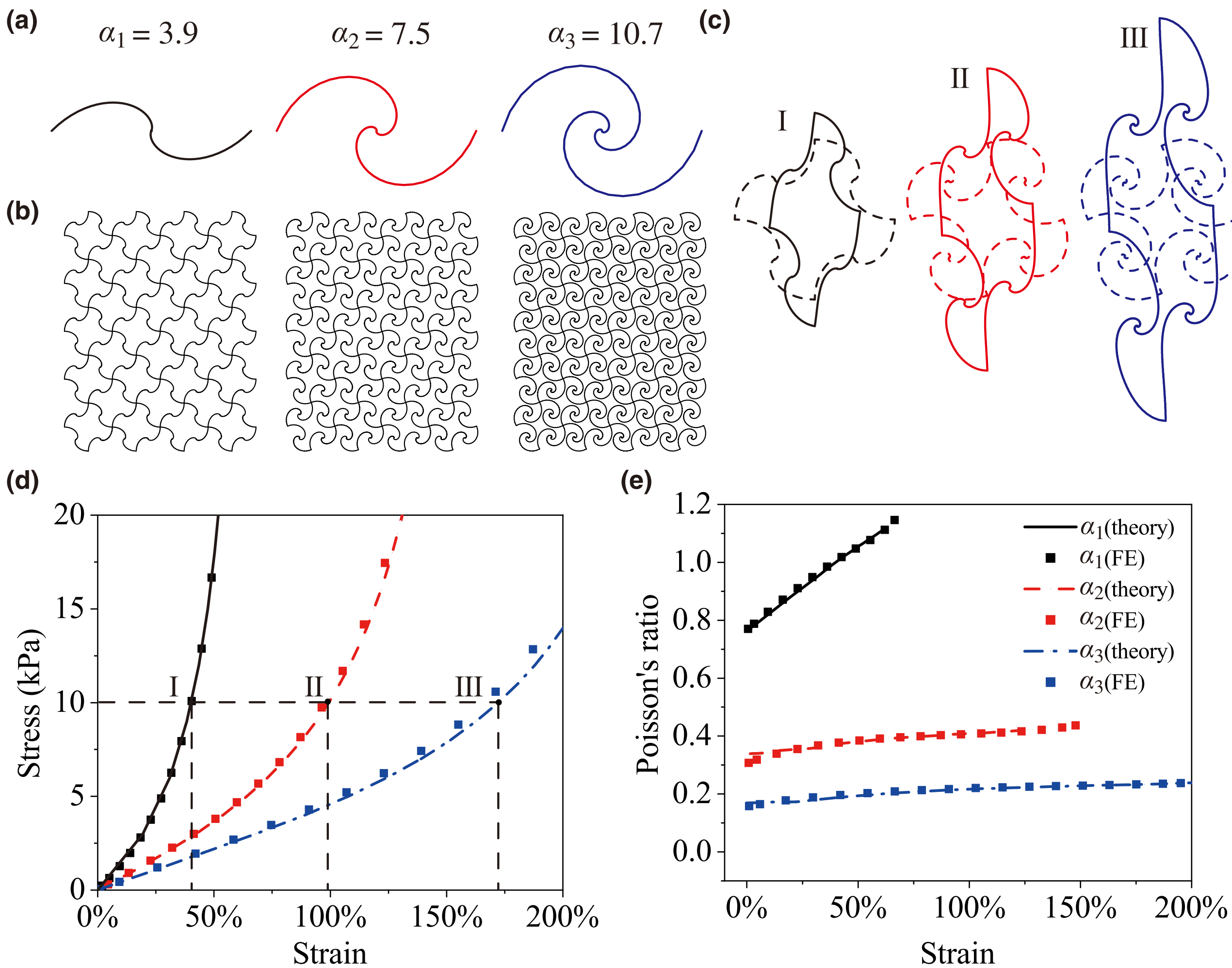

FIG. 5. Design of lattice by varying α in $R(\alpha)$. (a) Three microstructures are designed with $R(\alpha) = \alpha^3 + \alpha^2 + \alpha - 1, 0 \leq \alpha \leq \alpha_{\text{end}}$. $\alpha_{\text{end}} = \alpha_1(3.9), \alpha_2(7.5)$, and $\alpha_3(10.7)$ in the three structures, respectively. The designed rectangular lattices with 4×5 units are shown in (b). (c) shows the undeformed and deformed shapes of a representative unit of the rectangular lattice under $\sigma = 10$ kPa. (d),(e) show the variations of the stresses and Poisson's ratios on the strain for the three rectangular lattices, respectively. Theoretical and FE results are shown by the solid curves and markers, respectively.

strain further increases, the magnitude of Poisson's ratio increases a bit.

By varying n, the mechanical behavior of the lattices can be designed. For example, the object is to design a lattice with an axial strain of 60% when subjected to a uniaxial loading of 20 kPa. First, we can obtain the strain of the rectangular lattice under 20 kPa for $n = 0.5$ to 3, as shown in Fig. 6(d). The obtained strains are then plotted as a function of n in Fig. 6(f) and fitted using a second-order polynomial function. By setting the strain as 60% in the fitted model, the critical n is solved as $n = 1.78$, as shown by marker I. The corresponding initial and deformed shapes of the designed rectangular lattice under 20kPa are shown in Fig. 6(g). The measured strain is precisely 60%. Other designs by the parametric functions are shown in Figs. S5 and S8 within the Supplemental Material [52].

C. Design of bioinspired lattices

Nature provides various inspirations for structural design. One typical example is the curved structure, such as the plant tendrils [54] and wavy collagen fibers [55], which simultaneously possess low elastic moduli, large stretchability, and relatively high tensile strength. This type of structure has promoted the development of stretchable electronics by overcoming the limitations imposed by the natural rigidity and brittle properties of inorganic materials. Currently, it lacks a method to predict the mechanical behaviors of the lattice constructed by these bioinspired microstructures. Their mechanical behaviors can be predicted by a fitting method, which is a combination of curve fitting and the curvature and parametric functions. First, the nature-inspired structures are fitted to obtain the curvature or parametric functions. Next, the mechanical behaviors

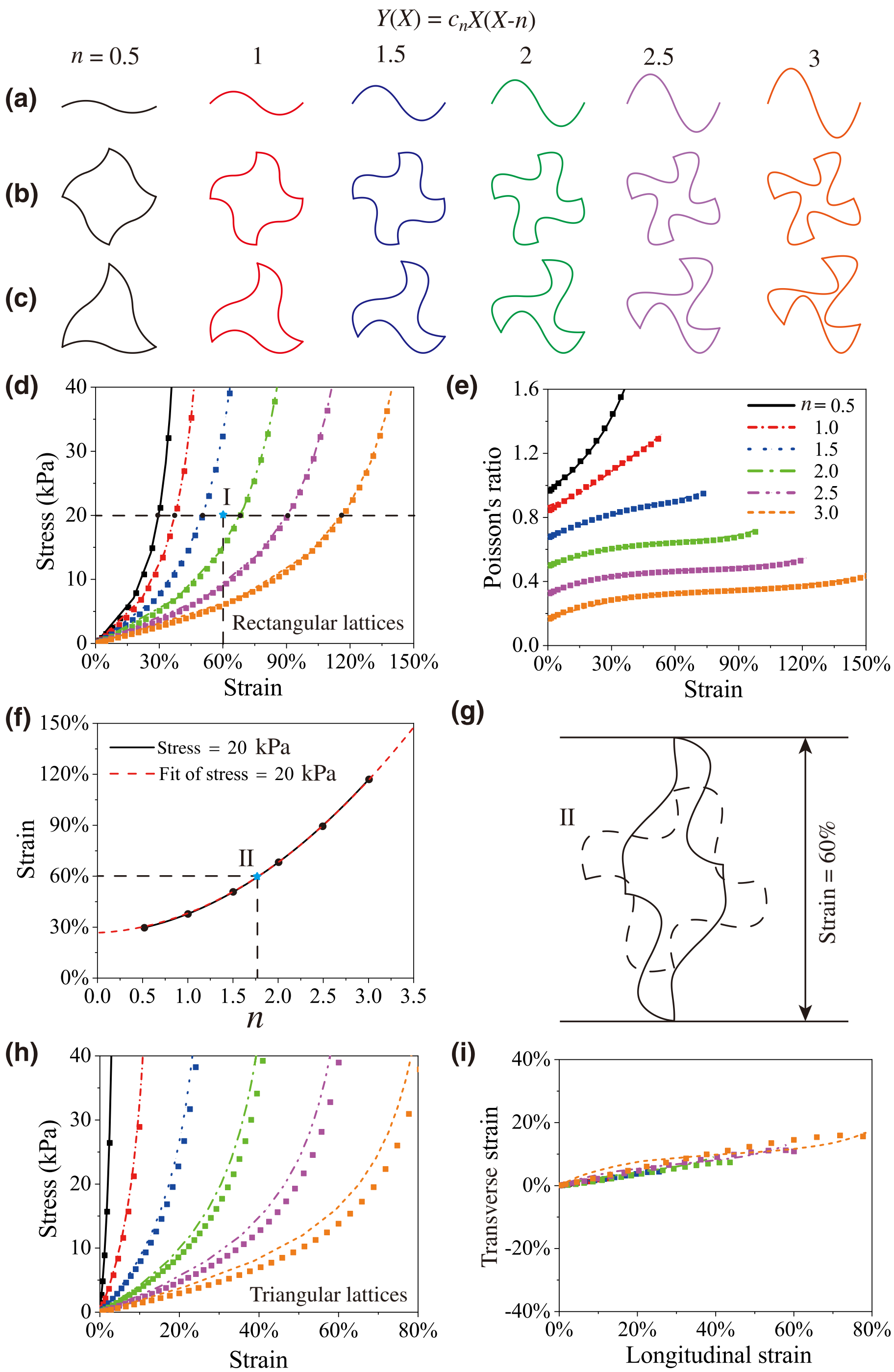

FIG. 6. Design of the lattices using different parametric functions. (a) Five curve functions, $Y(X) = c_nX(X-n)$, with $n = 0.5, 1, 1.5, 2, 2.5$, and 3, are used to construct the microstructures. The designed rectangular and triangular lattices are shown in (b),(c). (d) and (e) show the stress-strain and Poisson's ratio-strain curves of the rectangular lattices. Solid curves represent theoretical predictions and dotted curves are FE results. (f) shows the fitted axial strain versus n under $\sigma = 20$ kPa. For a desired axial strain 60%, the corresponding n is determined as 1.78 by the fitted curves. (g) shows the undeformed and deformed shapes of a representative unit with $n = 1.78$. (h),(i) show the stress-strain and transverse-longitudinal strain curves of the triangular lattices. Theoretical and FE results are shown by the solid curves and markers, respectively.

of the microstructure and lattice are investigated using the theoretical framework.

A bioinspired lattice is shown below as an example. Plant tendrils are ubiquitous and used by climbing plants for support and attachment due to their high stretchability [Fig. 7(a)]. Here we design a periodic rectangular lattice utilizing the structure of the plant tendrils. First, the curvature function of the plant tendril is obtained by fitting the curve as $R(a) = a^4 + 0.5a^3 + 2.4a^2 + 452.6a + 24.5$ [Fig. 7(a)]. The constructed microstructure and lattice are shown in Figs. 7(b) and 7(c). The theoretical stress-strain curves of the lattices are obtained and compared with the FE results of the same lattice and the rectangular lattice with straight beams. We can observe that using the plant tendril improves the stretchability by more than 10 times compared to the lattice constructed by straight beams under stress=32 kPa.

Both the parametric and the curvature functions are direct ways to construct microstructures, while the fitting method is inverse. If the trajectory of a curve is known

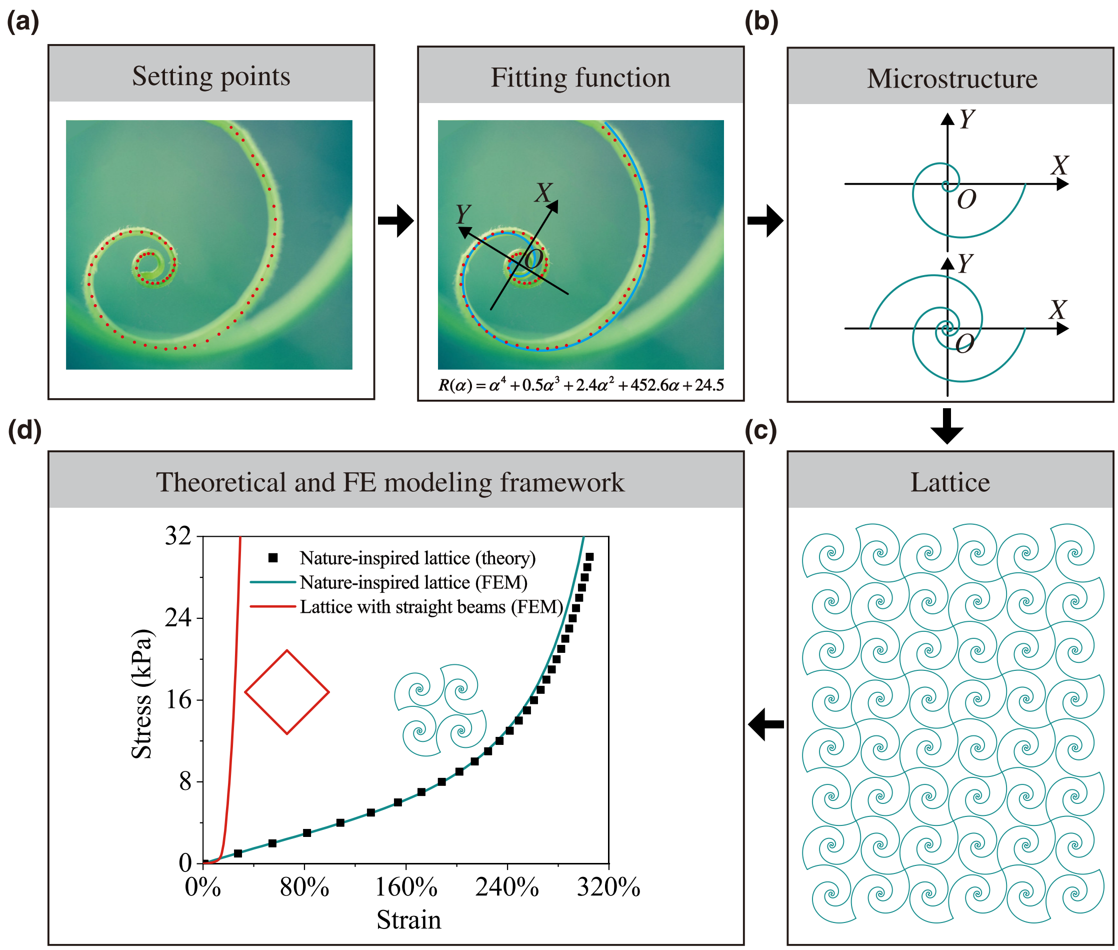

FIG. 7. Design of bioinspired lattices. (a) The plant tendrils with spiral shapes are used by climbing plants for support and attachment due to their high stretchability. The curve of the plant tendril is fitted using a polynomial curvature function. (b),(c) show the constructed microstructures and lattice. (d) The theoretical and FE simulated stress-strain curves of the lattice are compared with the FE simulated stress-strain curve of a rectangular lattice with straight beams.

but its particular function is unknown, the fitting function method offers a way to predict the mechanical behaviors of the constructed lattices. The curves are fitted using the curvature or parametric function first, and then the corresponding method is used to predict the mechanical behaviors of the constructed lattices. This method provides a more diverse design. However, it needs to overcome the challenges posed by the accuracy and complexity of fitting functions during inverse design.

D. Hydrogel reinforcement

The abilities of the designed lattices are explored to reinforce hydrogel, as shown in Fig. 8. The printed lattice structures are placed on a Teflon substrate and constrained by acrylic frames. Pregel solution is infused into the frames and then cured under UV light. The hydrogel is based on acrylamide (AAM)-PEGDA and can be stretched by more than 1000%. Detailed procedures are shown below. A hydrogel precursor is prepared by mixing AAM as monomer, PEGDA as the crosslinker, a water-soluble lithium phenyl-2,4,6-trimethylbenzoylphosphinate (Li-TPO) as the photoinitiator in water. The solution consists of 80% water, 20% AAM-PEGDA mixture with the PEGDA (700)/AAM mixing ratio of 0.625 wt%, and 0.5 wt% Li-TPO. Li-TPO is first added into deionized water, and the mixture is stirred by a magnetic stirrer for 10 min. AAM is then added into the mixture and it is stirred for 5 min until it has completely dissolved. PEGDA is added next.

Three rectangular lattices are designed, as shown by the insets in Fig. 8. The microstructures are constructed from the fitting curves 2, 3, and 4 in Fig. 8. (The detailed parametric functions and the mechanical behaviors of the constructed lattices are shown in Fig. S5 within the Supplemental Material [52].) The geometric parameters used are as follows: $w = 0.2$ mm and $d = 3$ mm.The experimental, theoretical, and FE stress-strain curves of the three

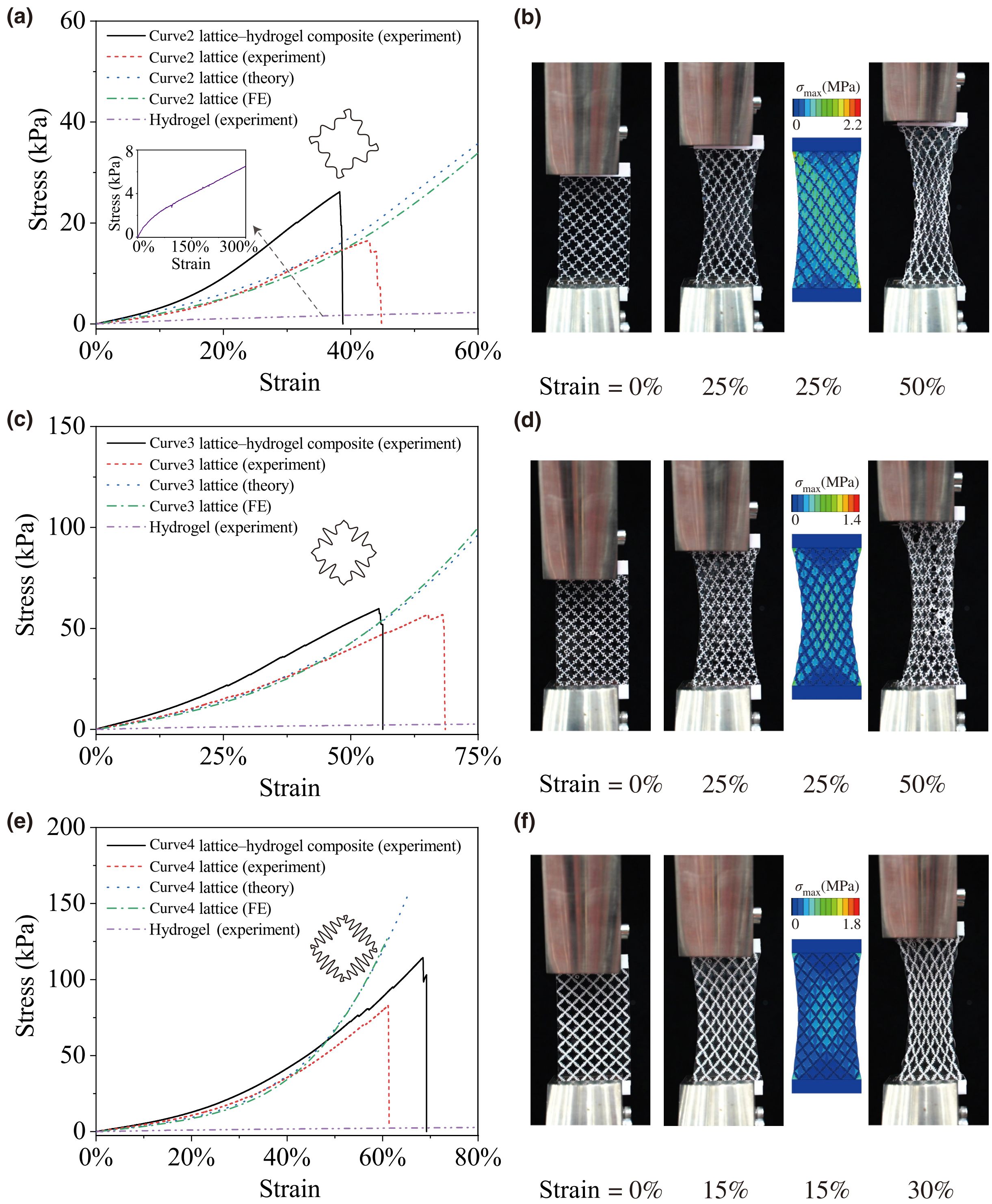

FIG. 8. Lattices as reinforcements for the hydrogel. Experimental, theoretical, and FE stress-strain curves for three rectangular lattice structures. The three microstructures are constructed from (a) curve 2, (c) curve 3, and (e) curve 4 in Fig. S5 within the Supplemental Material [52]. The experimental stress-strain curves of the rectangular lattice-hydrogel composite are also shown. The insets show the periodic units of the lattices. The snapshots of the lattice-hydrogel composite at different strains are shown in (b),(d), and (f). Distributions of the maximum principal stress (σ_{max}) are shown.

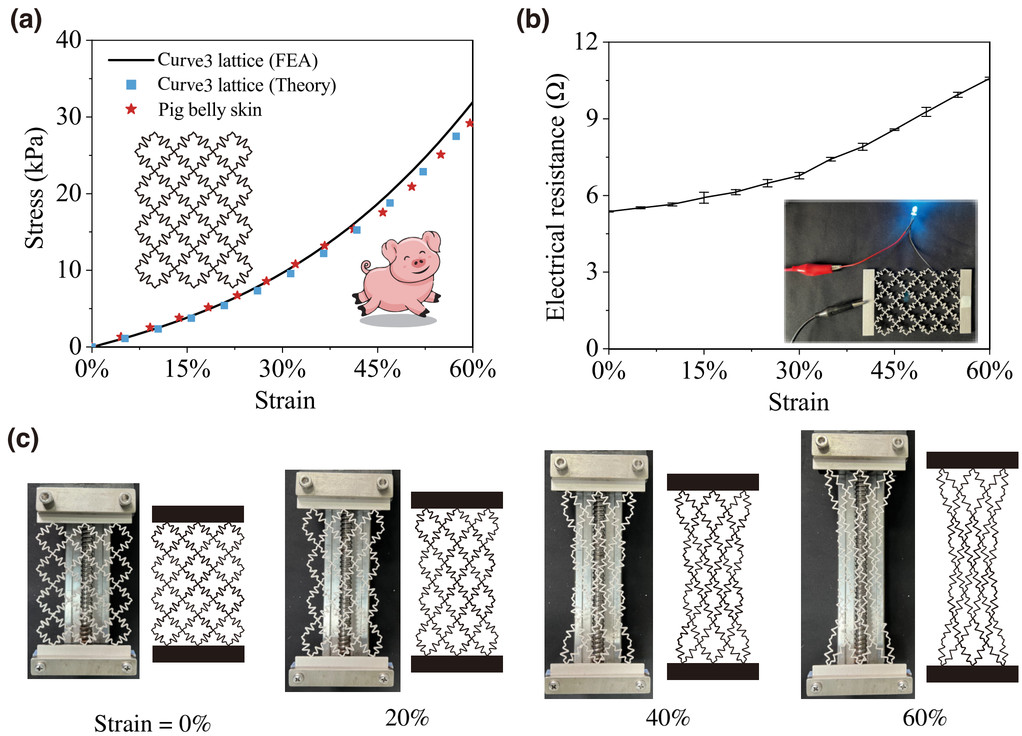

FIG. 9. Demonstration of the biomimetic soft lattice sensor for stretchable electronics. (a) The soft lattice is designed to match the stress-strain curves of the pig belly skin. The lattice structure is shown in the inset. (b) The dependence of the electrical resistance on the axial strain of the biomimetic lattice coated with a thin layer of silver. (c) Optical images of conductive biomimetic lattice and FEM results at different applied strains.

rectangular lattices are shown in Figs. 8(a), 8(c), and 8(e). The experimental stress-strain curves of pure hydrogel and the lattice-hydrogel composites are also shown.

The hydrogel is significantly reinforced by the lattice structure. Young's moduli of the lattice-hydrogel composites are in the orders of 100 kPa, while that of the hydrogel is a few kPa. By using different lattice structures, the failure strain of the lattice-hydrogel composite also varies. The snapshots of the lattice-hydrogel composites at different strains are shown in Figs. 8(b), 8(d), and 8(f). It can be seen that the interfacial bonding between the hydrogel and the lattice are strong enough.

FE simulations are conducted for the lattice-hydrogel composite (Video S4 within the Supplemental Material [52]). The deformed shapes and strain contours at strains = 25% for lattices 2 and 3, and strain = 15% for lattice 4 are shown in Fig. 8. It can be seen that different embedded lattices can cause various strain distributions. For example, the strain distribution is asymmetric for lattice 2, while the strain distributions are almost symmetric for lattices 3 and 4. The common point is that the largest strain always appears at the corner or the center of the lattice-hydrogel composites. This phenomenon agrees with the experiments, in which the composites fail at the corner or the center.

E. Biomimetic soft lattice sensor

To show the potential application of the proposed theoretical method, a biomimetic soft sensor with large stretchability, bionic stress-strain matching, and programmable deformed shapes is designed. Rational biomimetic designs of periodic lattices can match the nonlinear J-shaped stress-strain curves of various soft biological tissues and thus enable natural, comfortable integration of stretchable electronics with biological tissues. A lattice sensor is designed that can reproduce the nonlinear mechanical responses of the pig belly skin, as shown in Fig. 9. The rectangular lattice is constructed from curve 3. By choosing the wavy microstructure, large stretchability is ensured. To match the stress-strain curves of the pig belly skin [56], the theoretical framework is used and the geometric parameters are calculated as $w = 0.16$ mm and $d = 2$ mm. The theoretical and FE stress-strain curves are compared with the experimental stress-strain curves of the pig belly skin in Fig. 9(a). We can observe that the stress-strain curves of the lattice agree well with the pig belly skin. Therefore, it ensures comfortable interactions.

The conductive lattice is fabricated by coating with a thin layer of silver. Its resistance is measured under different tensile strains. One end of the lattice is fixed during the measurement, and the other end is clamped on a

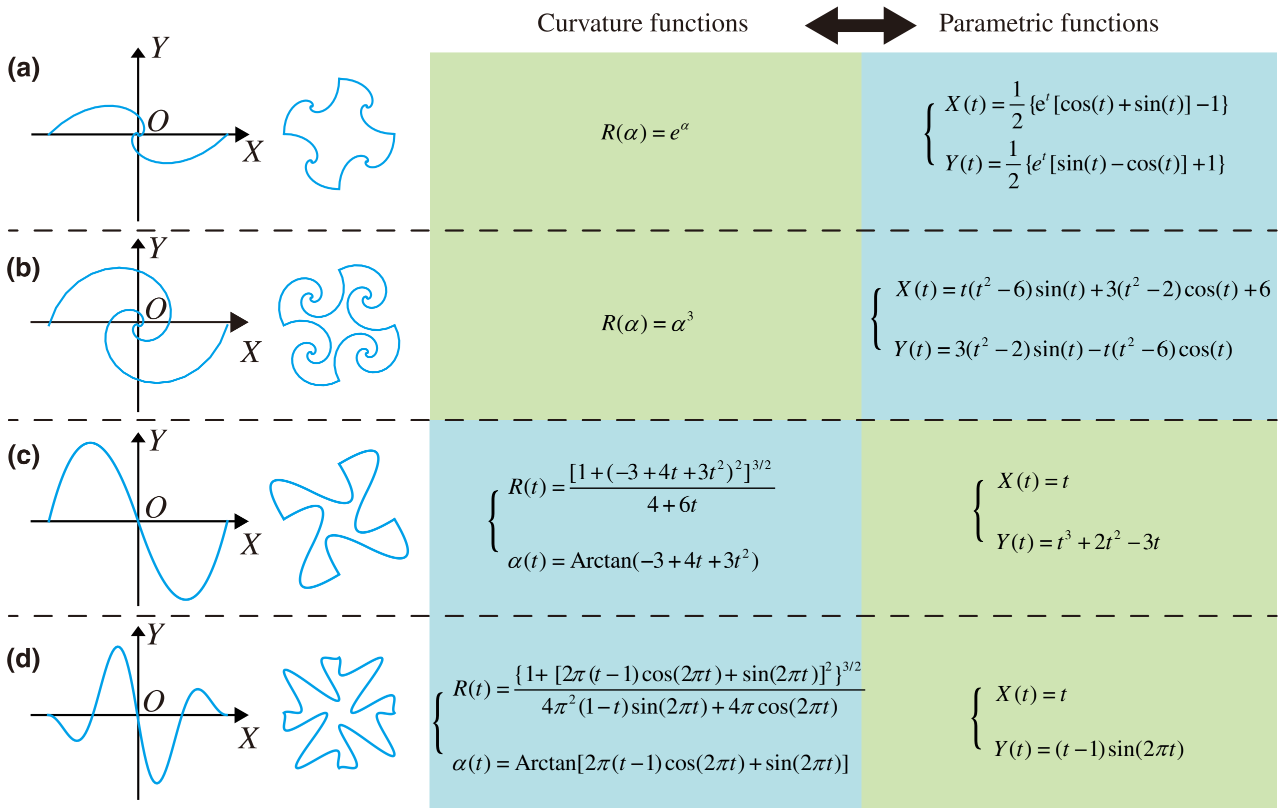

FIG. 10. The curvature and parametric functions for spiral and wavy curves. The curvature functions are commonly used to construct spiral curves with one-to-one mapping from the α to R [(a) and (b)]. The parametric functions are used to generate wavy curves with one-to-one mapping from X to Y (c),(d). The parametric and curvature functions can be converted to each other using coordinate transformations.

stepper motor (ST42H4809, Sutai) to generate linear displacement. The resistance of the conductive biomimetic lattice is measured by a precision LCR meter (Keysight E4980AAL) with a frequency of 1kHz. It shows the resistance of the conductive biomimetic lattices exhibits a twofold increase under strain = 60% due to the elongation and thinning of the silver coating. The optical images of conductive biomimetic lattice and FEM results are shown in Fig. 9(c) to illustrate the predictable deformed shapes visually. The developed lattice sensor, with large stretchability, bionic stress-strain matching, and programmable deformed shapes, holds promise for biointegrated devices and health monitoring applications (Fig. S9 within the Supplemental Material [52]).

VI. CONCLUSIONS

The curvature function is commonly used to construct spiral functions with one-to-one mapping from the slope angle α to the instant radius R, while the parametric function is suitable to generate wavy curves with one-to-one mapping from X to Y. The curvature function $R(a)$ describes the relationship between the instant radius R and the slope angle α. Many curves, such as spiral and logarithmic spiral, can be characterized by a relatively simple curvature function, whereas their parametric function is much more intricate [Figs. 10(a) and 10(b)]. In contrast, the curvature function is inefficient for the wavy curves as the relationship between R and α is complex, while the parametric functions are suitable due to the one-to-one mapping from X to Y [Figs. 10(c) and 10(d)]. It should be noted that parametric and curvature functions can be converted using coordinate transformations.

This study presents a universal model for lattices constructed by various microstructures. It investigates the mechanical behaviors of the rectangular, triangular, and symmetric rectangular lattices constructed by microstructures with varying curvatures using a combination of theoretical, experimental, and FE methods. Unlike previous studies where the microstructures are mainly simple geometries such as straight, horseshoe, or serpentine structures with constant curvatures, microstructures with varying curvatures are used in this work. Two methods are demonstrated to construct the microstructures: (1) using the relation of the instant radius with the slope angle and (2) using the parametric function. The mechanical behavior of the lattice can be predicted once the curve function of the microstructure is determined. Results show that the elastic moduli, stretchabilities, and Poisson's ratios can be tailored by the rational design of the lattice structures. Lattices with dramatically increased stretchability can be designed by using densely curled microstructures. By combining curve fitting and curvature and parametric functions, the mechanical behaviors of lattices constructed by bioinspired microstructures can be predicted. Demonstrations of the designed lattice as a hydrogel reinforcement and biomimetic soft strain sensor are shown. The proposed method overcomes the limitation that the microstructures have to follow a particular pattern and can be extended to study lattices constructed by microstructures with not only varying shapes but also varying cross sections and varying Young's moduli. Lattice constructed by a combination of different microstructures can also be studied using the proposed method as future work. This work could aid the design of hierarchical lattice and have potential applications in tissue engineering, stretchable electronics, and soft robotics.

ACKNOWLEDGMENTS

D.W. acknowledges support from the National Natural Science Foundation of China (Grant No. 51905336) and the Shanghai Sailing Program (Grant No. 19YF1423000). G.Y.Gu acknowledges support from the National Natural Science Foundation of China (Grant No. 52025057). B.Z. acknowledges support from Natural Science Basic Research Program of Shanxi (Program No. 2020JQ-174).

[1] J. L. Silverberg, A. A. Evans, L. McLeod, R. C. Hayward, T. Hull, C. D. Santangelo, and I. Cohen, Using origami design principles to fold reprogrammable mechanical metamaterials, science **345**, 647 (2014).

[2] L. Jin, A. E. Forte, B. Deng, A. Rafsanjani, and K. Bertoldi, Kirigami-inspired inflatables with programmable shapes, Adv. Mater. **32**, 2001863 (2020).

[3] H. Yasuda and J. Yang, Reentrant Origami-Based Metamaterials with Negative Poisson's Ratio and Bistability, Phys. Rev. Lett. **114**, 185502 (2015).

[4] M.-S. Pham, C. Liu, I. Todd, and J. Lertthanasarn, Damage-tolerant architected materials inspired by crystal microstructure, Nature **565**, 305 (2019).

[5] S. Roh, L. B. Okello, N. Golbasi, J. P. Hankwitz, J. A.-C. Liu, J. B. Tracy, and O. D. Velev, 3d-printed silicone soft architectures with programmed magneto-capillary reconfiguration, Adv. Mater. Technol. **4**, 1800528 (2019).

[6] K. Bertoldi, V. Vitelli, J. Christensen, and M. Van Hecke, Flexible mechanical metamaterials, Nat. Rev. Mater. **2**, 17066 (2017).

[7] L. Ai and X.-L. Gao, Micromechanical modeling of 3d printable interpenetrating phase composites with tailorable effective elastic properties including negative poisson's ratio, J. Micromech. Mol. Phys. **2**, 1750015 (2017).

[8] D. Restrepo, N. D. Mankame, and P. D. Zavattieri, Programmable materials based on periodic cellular solids. Part I: Experiments, Int. J. Solids Struct. **100**, 485 (2016).

[9] D. Restrepo, N. D. Mankame, and P. D. Zavattieri, Programmable materials based on periodic cellular solids. Part II: Numerical analysis, Int. J. Solids Struct. **100**, 505 (2016).

[10] Q. Zhang, X. Yang, P. Li, G. Huang, S. Feng, C. Shen, B. Han, X. Zhang, F. Jin, and F. Xu, *et al.*, Bioinspired engineering of honeycomb structure–using nature to inspire human innovation, Prog. Mater. Sci. **74**, 332 (2015).

[11] Y. Tao, W. Li, K. Wei, S. Duan, W. Wen, L. Chen, Y. Pei, and D. Fang, Mechanical properties and energy absorption of 3d printed square hierarchical honeycombs under in-plane axial compression, Compos. Part B: Eng. **176**, 107219 (2019).

[12] M. C. Fernandes, J. Aizenberg, J. C. Weaver, and K. Bertoldi, Mechanically robust lattices inspired by deep-sea glass sponges, Nat. Mater. **20**, 237 (2021).

[13] C. Storm, J. J. Pastore, F. C. MacKintosh, T. C. Lubensky, and P. A. Janmey, Nonlinear elasticity in biological gels, Nature **435**, 191 (2005).

[14] P. A. Janmey, M. E. McCormick, S. Rammensee, J. L. Leight, P. C. Georges, and F. C. MacKintosh, Negative normal stress in semiflexible biopolymer gels, Nat. Mater. **6**, 48 (2007).

[15] R. E. Shadwick, Mechanical design in arteries, J. Exp. Biol. **202**, 3305 (1999).

[16] Y.-c. Fung, *A First Course in Continuum Mechanics* (Prentice-Hall Inc, Englewood Cliffs, 1977).

[17] A. N. Annaidh, K. Bruyère, M. Destrade, M. D. Gilchrist, and M. Otténio, Characterization of the anisotropic mechanical properties of excised human skin, J. Mech. Behav. Biomed. Mater. **5**, 139 (2012).

[18] A Mathematical Model of Lung Parenchyma, J. Biomech. Eng. **102**, 124 (1980).

[19] J. Ø. Hjortdal, Extensibility of the normo-hydrated human cornea, Acta Ophthalmol. Scand. **73**, 12 (1995).

[20] J. V. Shah and P. A. Janmey, Strain hardening of fibrin gels and plasma clots, Rheol. Acta. **36**, 262 (1997).

[21] P. F. Egan, K. A. Shea, and S. J. Ferguson, Simulated tissue growth for 3d printed scaffolds, Biomech. Model. Mechanobiol. **17**, 1481 (2018).

[22] M. Fantini, M. Curto, and F. De Crescenzio, A method to design biomimetic scaffolds for bone tissue engineering based on voronoi lattices, Virtual Phys. Prototyp. **11**, 77 (2016).

[23] S. Yao, P. Ren, R. Song, Y. Liu, Q. Huang, J. Dong, B. T. O'Connor, and Y. Zhu, Nanomaterial-enabled flexible and stretchable sensing systems: Processing, integration, and applications, Adv. Mater. **32**, 1902343 (2020).

[24] X. Zhao, J. Kim, C. A. Cezar, N. Huebsch, K. Lee, K. Bouhadir, and D. J. Mooney, Active scaffolds for on-demand drug and cell delivery, Proc. Nat. Acad. Sci. **108**, 67 (2011).

[25] M. Castilho, G. Hochleitner, W. Wilson, B. van Rietbergen, P. D. Dalton, J. Groll, J. Malda, and K. Ito, Mechanical behavior of a soft hydrogel reinforced with three-dimensional printed microfibre scaffolds, Sci. Rep. **8**, 1245 (2018).

[26] J. Visser, F. P. Melchels, J. E. Jeon, E. M. Van Bussel, L. S. Kimpton, H. M. Byrne, W. J. Dhert, P. D. Dalton, D. W. Hutmacher, and J. Malda, Reinforcement of hydrogels using three-dimensionally printed microfibres, Nat. Commun. **6**, 6933 (2015).
[27] J. A. Fan, W.-H. Yeo, Y. Su, Y. Hattori, W. Lee, S.-Y. Jung, Y. Zhang, Z. Liu, H. Cheng, and L. Falgout, *et al.*, Fractal design concepts for stretchable electronics, Nat. Commun. **5**, 3266 (2014).
[28] Y. Ma, X. Feng, J. A. Rogers, Y. Huang, and Y. Zhang, Design and application of 'j-shaped'stress–strain behavior in stretchable electronics: A review, Lab Chip **17**, 1689 (2017).
[29] H. Chen, F. Zhu, K.-I. Jang, X. Feng, J. A. Rogers, Y. Zhang, Y. Huang, and Y. Ma, The equivalent medium of cellular substrate under large stretching, with applications to stretchable electronics, J. Mech. Phys. Solids **120**, 199 (2018).
[30] J. Liu, H. Song, and Y. Zhang, Toward imperfection-insensitive soft network materials for applications in stretchable electronics, ACS Appl. Mater. Interfaces **11**, 36100 (2019).
[31] A. Rafsanjani, K. Bertoldi, and A. R. Studart, Programming soft robots with flexible mechanical metamaterials, Sci. Robotics **4**, eaav7874 (2019).
[32] S. Choi, H. Lee, R. Ghaffari, T. Hyeon, and D.-H. Kim, Recent advances in flexible and stretchable bio-electronic devices integrated with nanomaterials, Adv. Mater. **28**, 4203 (2016).
[33] N. G. Cheng, A. Gopinath, L. Wang, K. Iagnemma, and A. E. Hosoi, Thermally tunable, self-healing composites for soft robotic applications, Macromol. Mater. Eng. **299**, 1279 (2014).
[34] C. Yang, M. Boorugu, A. Dopp, J. Ren, R. Martin, D. Han, W. Choi, and H. Lee, 4d printing reconfigurable, deployable and mechanically tunable metamaterials, Mater. Horiz. **6**, 1244 (2019).
[35] K.-I. Jang, H. U. Chung, S. Xu, C. H. Lee, H. Luan, J. Jeong, H. Cheng, G.-T. Kim, S. Y. Han, and J. W. Lee, *et al.*, Soft network composite materials with deterministic and bio-inspired designs, Nat. Commun. **6**, 6566 (2015).
[36] Y. Chen, Z. Jia, and L. Wang, Hierarchical honeycomb lattice metamaterials with improved thermal resistance and mechanical properties, Compos. Struct. **152**, 395 (2016).
[37] L. Meng, J. Shi, C. Yang, T. Gao, Y. Hou, L. Song, D. Gu, J. Zhu, P. Breitkopf, and W. Zhang, An emerging class of hyperbolic lattice exhibiting tunable elastic properties and impact absorption through chiral twisting, Extreme Mech. Lett. **40**, 100869 (2020).
[38] Y. Chen, T. Li, F. Scarpa, and L. Wang, Lattice Metamaterials with Mechanically Tunable Poisson's Ratio for Vibration Control, Phys. Rev. Appl. **7**, 024012 (2017).
[39] Q. Ma and Y. Zhang, Mechanics of fractal-inspired horseshoe microstructures for applications in stretchable electronics, J. Appl. Mech. **83**, 11 (2016).
[40] Y. Su, S. Wang, Y. Huang, H. Luan, W. Dong, J. A. Fan, Q. Yang, J. A. Rogers, and Y. Huang, Elasticity of fractal inspired interconnects, small **11**, 367 (2015).
[41] Z. Cui, Y. Han, Q. Huang, J. Dong, and Y. Zhu, Electrohydrodynamic printing of silver nanowires for flexible and stretchable electronics, Nanoscale **10**, 6806 (2018).
[42] D. F. Fernandes, C. Majidi, and M. Tavakoli, Digitally printed stretchable electronics: A review, J. Mater. Chem. C **7**, 14035 (2019).
[43] Y. Cao, G. Zhang, Y. Zhang, M. Yue, Y. Chen, S. Cai, T. Xie, and X. Feng, Direct fabrication of stretchable electronics on a polymer substrate with process-integrated programmable rigidity, Adv. Funct. Mater. **28**, 1804604 (2018).
[44] S. Janbaz, F. Bobbert, M. Mirzaali, and A. Zadpoor, Ultra-programmable buckling-driven soft cellular mechanisms, Mater. Horiz. **6**, 1138 (2019).
[45] A. G. Mark, S. Palagi, T. Qiu, and P. Fischer, in *2016 IEEE international conference on robotics and automation (ICRA)* (Ieee, 2016), p. 4951.
[46] Q. Ma, H. Cheng, K.-I. Jang, H. Luan, K.-C. Hwang, J. A. Rogers, Y. Huang, and Y. Zhang, A nonlinear mechanics model of bio-inspired hierarchical lattice materials consisting of horseshoe microstructures, J. Mech. Phys. Solids **90**, 179 (2016).
[47] Z. Fan, Y. Zhang, Q. Ma, F. Zhang, H. Fu, K.-C. Hwang, and Y. Huang, A finite deformation model of planar serpentine interconnects for stretchable electronics, Int. J. Solids Struct. **91**, 46 (2016).
[48] Y. Zhang, H. Fu, S. Xu, J. A. Fan, K.-C. Hwang, J. Jiang, J. A. Rogers, and Y. Huang, A hierarchical computational model for stretchable interconnects with fractal-inspired designs, J. Mech. Phys. Solids **72**, 115 (2014).
[49] J. Liu and Y. Zhang, Soft network materials with isotropic negative poisson's ratios over large strains, Soft Matter **14**, 693 (2018).
[50] D. Wang, Y. Xiong, B. Zhang, Y.-F. Zhang, D. Rosen, and Q. Ge, Design framework for mechanically tunable soft biomaterial composites enhanced by modified horseshoe lattice structures, Soft Matter **16**, 1473 (2020).
[51] K. Lin and C. Lin, Finite deformation of 2-d laminated curved beams with variable curvatures, Int. J. Non-Linear Mech. **46**, 1293 (2011).
[52] See Supplemental Material at http://link.aps.org/supplemental/10.1103/PhysRevApplied.17.044032, which includes Refs. [57–62], supporting videos, analytical explorations, details of the FE simulations, and descriptions of the experiments.
[53] G. N. Greaves, A. Greer, R. S. Lakes, and T. Rouxel, Poisson's ratio and modern materials, Nat. Mater. **10**, 823 (2011).
[54] W. Wang, C. Li, M. Cho, and S.-H. Ahn, Soft tendril-inspired grippers: Shape morphing of programmable polymer–paper bilayer composites, ACS Appl. Mater. Interfaces **10**, 10419 (2018).
[55] J. M. Caves, V. A. Kumar, W. Xu, N. Naik, M. G. Allen, and E. L. Chaikof, Microcrimped collagen fiber-elastin composites, Adv. Mater. **22**, 2041 (2010).
[56] S. S. Sheiko and A. V. Dobrynin, Architectural code for rubber elasticity: From supersoft to superfirm materials, Macromolecules **52**, 7531 (2019).

[57] S. Liu and L. Li, Ultrastretchable and self-healing double-network hydrogel for 3d printing and strain sensor, ACS Appl. Mater. Interfaces **9**, 26429 (2017).

[58] H. Li, H. Zheng, Y. J. Tan, S. B. Tor, and K. Zhou, Development of an ultrastretchable double-network hydrogel for flexible strain sensors, ACS Appl. Mater. Interfaces **13**, 12814 (2021).

[59] Y.-Z. Zhang, K. H. Lee, D. H. Anjum, R. Sougrat, Q. Jiang, H. Kim, and H. N. Alshareef, Mxenes stretch hydrogel sensor performance to new limits, Sci. Adv. **4**, eaat0098 (2018).

[60] C. S. Boland, C. Ó. Coileáin, S. Wagner, J. B. McManus, C. P. Cullen, M. C. Lemme, G. S. Duesberg, and N. McEvoy, Ptse2 grown directly on polymer foil for use as a robust piezoresistive sensor, 2D Mater. **6**, 045029 (2019).

[61] X. Cheng and Y. Zhang, Nonlinear compressive deformations of buckled 3d ribbon mesostructures, Extreme Mech. Lett. **42**, 101114 (2021).

[62] R. Herbert, H.-R. Lim, and W.-H. Yeo, Printed, soft, nanostructured strain sensors for monitoring of structural health and human physiology, ACS Appl. Mater. Interfaces **12**, 25020 (2020).